Journal of Colloid and Interface Science 428 (2014) 133–140

Contents lists available at ScienceDirect

Journal of Colloid and Interface Science

www.elsevier.com/locate/jcis

Electrochemical properties of boron-doped ordered mesoporous carbon as electrocatalyst and Pt catalyst support

Anaclet Nsabimana, Xiangjie Bo *, Yufan Zhang, Mian Li, Ce Han, Liping Guo *

Faculty of Chemistry, Northeast Normal University, 130024 Changchun, People's Republic of China

ARTICLE INFO

Article history:
Received 19 March 2014
Accepted 21 April 2014
Available online 8 May 2014

Keywords:
Ordered mesoporous carbon
Boron doping
Platinum nanoparticles
Biosensor
Methanol oxidation

ABSTRACT

The electrochemical properties of boron-doped ordered mesoporous carbon (BOMC) as an electrode material and Pt catalyst support were investigated. The BOMC was synthesized and its structure was examined by transmission electron microscopy (TEM), scanning electron microscopy, nitrogen adsorption–desorption, X-ray diffraction, Raman spectroscopy, and X-ray photoelectron spectroscopy (XPS). More defective sites were introduced into OMC by the doping of boron. Six electroactive compounds were employed to investigate their electrochemical responses on BOMC and OMC modified glassy carbon electrodes. The BOMC, with more defective sites, exhibited high activity toward the electroactive compounds. The property of BOMC of supporting platinum nanoparticle catalyst was examined. Pt nanoparticles were loaded onto BOMC and OMC, and this was confirmed by TEM, XPS and thermogravimetric analysis. Pt nanoparticles with an average diameter of 2.62 nm were deposited on BOMC. The doping of boron into OMC facilitates the dispersion of Pt nanoparticles. Pt nanoparticles supported on BOMC (Pt-BOMC) and Pt nanoparticles supported on OMC (Pt-OMC) were electrochemically characterized. The electrocatalytic activity of Pt-BOMC toward methanol oxidation reaction was compared with that of Pt-OMC and commercial Pt-C catalyst. The results show that the electrocatalytic activity of BOMC is significantly higher than that of other used catalysts.

1. Introduction

Ordered mesoporous carbon (OMC), since its discovery in 1999 [1], has been receiving much attention owing to its properties such as extremely well-ordered pore structure, high specific pore volume, high specific surface area, tunable pore diameters in the mesopore range, large adsorption capacities, low electron-transfer resistance, high thermal and mechanical stabilities, and chemical inertness [2–7]. These properties make it suitable for applications in molecule separation [8], adsorption [9,10], catalysis [11,12], sensors [13–15], energy storage and capacitors [16–18]. Several methods have been used to synthesize OMC resulting in different types of ordered mesoporous structures. For example, CMK-3 was synthesized using SBA-15 silica as the template and sucrose as the carbon source, giving the ordered structure of the CMK-3 carbon which is exactly an inverse replica without involving structural transformation during the removal of the silica template [19]. On the basis of the properties of OMC like oxygen-containing functional groups, edge plane defect sites, large surface area, widely open and ordered structure, many electrochemical sensors were made [2,5,20]. Its ability of loading active biomolecules and catalysts was used to make several biosensors by incorporating active molecules in OMC or immobilization of biomolecules on OMC. The functionalization of OMC by noble metal nanoparticles [21,22], inorganic mediators [23], organometallic catalysts [24,25], organic redox mediators [26,27], metal oxides or sulfides [28,29], and ionic liquids [30,31] was used to improve the catalytic properties of OMC. Recently, in order to enhance further the materials properties, much research on doping OMC by heteroatoms was adopted.

Metal-free heteroatom-incorporated OMC attracted much attention because they are cheap, highly active and selective electrocatalysts [32–35]. Much research on carbon materials has shown that the modification with electron-donating or electron-withdrawing elements, such as N, P, B, and O, could change the electronic properties of carbons and produce additional functional groups on the carbon surface, and as a result, greatly enhance the electrochemical performance of carbon materials [32–36]. For example, Yang and coworkers synthesized phosphorus-doped ordered mesoporous carbons (POMC) with different lengths, using a nanocasting method of SBA-15 mesoporous silica with different sizes as template and triphenylphosphine and phenol as phosphorus and carbon sources, respectively. The obtained POMC with a small amount of P doping was demonstrated as a metal-free

* Corresponding authors. Fax: +86 0431 85099762 (L. Guo).
E-mail addresses: baoxj133@nenu.edu.cn (X. Bo), guolp078@nenu.edu.cn (L. Guo).

http://dx.doi.org/10.1016/j.jcis.2014.04.044
0021-9797/

electrode with excellent electrocatalytic activity for oxygen reduction reaction, coupled with much enhanced stability and alcohol tolerance compared to those of platinum by four-electron pathway in alkaline medium [32]. Among these various heteroatoms, boron is an element, bearing three valence electrons.

Owing to its three valence electrons, oxidation-resistance, and being favorable to graphitization, boron is considered as a good dopant [37]. After its incorporation in carbon materials, there is remarkable improvement in the electrochemical activities of the resulting product. The existence of B–C bonds in the carbon framework can lower the Fermi level of the structure and then tune the properties of oxygen chemisorption and electrochemistry for redox reactions [35,37–40]. The previous studies showed that the existence of boron restricts the C–O_2 reaction because boron can act as an electron acceptor and reduce the electron density at the carbon crystallite edges [38]. The boron-doped carbon materials such as boron doped diamond [41,42], graphene [43,44], carbon nanotube [45–47], and porous carbon [33–35,37,40], exhibited good performance for different applications. Despite the good electrochemical performance of OMC compared with other carbon materials and the advantages of boron doping, to date, there have been only few studies on the electrochemical applications of boron-doped ordered mesoporous carbon (BOMC) [34,35,39].

In this work, the electrochemical properties of BOMC as an electrode material and Pt catalyst support were investigated. The electrochemical and catalytic performance of BOMC was studied and compared with that of OMC. We focused on the response at BOMC-modified glassy carbon electrode (BOMC/GCE) and OMC-modified glassy carbon electrode (OMC/GCE) for the electrocatalysis of six electroactive compounds and biomolecules (ascorbic acid (AA), dopamine (DA), uric acid (UA), β-nicotinamide adenine dinucleotide (NADH), hydrogen peroxide (H_2O_2), and glucose). The previous research showed that boron doping can introduce active sites on carbon nanomaterials, acting as the anchoring sites to support catalyst nanoparticles [47]. In this work, the platinum nanoparticles were incorporated in the pores of BOMC. The electrocatalytic performance of the obtained Pt nanoparticles supported on BOMC (Pt-BOMC), for direct methanol oxidation reaction, was investigated by comparing its activity with that of Pt nanoparticles supported on OMC (Pt-OMC) and commercial Pt-C catalyst.

2. Experimental

2.1. Reagents

Pluronic P123 (non-ionic triblock copolymer, $EO_{20}PO_{70}EO_{20}$), Nafion (5 wt.%), NADH, DA, AA and UA were purchased from Sigma–Aldrich (MO, USA). H_2O_2 was obtained from Beijing Chemical Co. (China). Glucose, methanol, sucrose and 4-hydroxyphenylboronic acid were purchased from Sinopharm Chemical Reagent Co., Ltd. China. All other used reagents were of analytical grade and used as received without further purification. A 0.1 M pH 7.4 phosphate buffer solution (PBS), prepared using a combination of NaH_2PO_4, Na_2HPO_4 and H_3PO_4, was used in all electrochemical studies, except in methanol oxidation reactions where 0.5 M H_2SO_4 was used.

2.2. Apparatus and measurements

Cyclic voltammetry (CV) and amperometric *i–t* curves were performed with a CHI 830B electrochemical workstation (CH Instruments, Shanghai Chenhua Instrument Corporation, China). The chronoamperometry for methanol oxidation was conducted using a Par 2273 Potentiostats-Electrochemistry Workstation. A three-electrode configuration was employed, with a modified glassy carbon electrode (GCE, 3.0 mm in diameter) serving as the working electrode, and Ag/AgCl (in saturated KCl solution) and platinum wire serving as the reference and counter electrodes, respectively. All potentials in this work were measured and reported versus Ag/AgCl. The electrochemical reactions were carried out at room temperature. Philips XL-30 ESEM was used to determine the morphology of product. The samples were cast on indium tin oxide glass for SEM measurement. Transmission electron microscopy (TEM) images were obtained using a JEM-2100F transmission electron microscope (JEOL, Japan) operating at 200 kV. The nitrogen adsorption–desorption isotherm was performed on an ASAP 2020 (Micromeritics, USA). The Brunauer–Emmett–Teller (BET) method was utilized to calculate the specific surface area. The pore size distribution was derived from the adsorption branch by using the Barrett–Joyner–Halenda model. X-ray diffraction (XRD) pattern was obtained on an X-ray D/max-2200vpc (Rigaku Corporation, Japan) instrument operated at 40 kV and 20 mA using Cu Kα radiation (k = 0.15406 nm). Raman spectra were obtained using a confocal microprobe Raman system (HR800, Jobin Yvon). X-ray photoelectron spectroscopy (XPS) was measured using Thermo ESCA LAB spectrometer (USA). The binding energies were calibrated by using the containment carbon (C1s = 284.6 eV). Thermogravimetric analysis (TGA) was performed on a PerkinElmer Diamond TG Analyzer and the Pt content was determined by TGA.

2.3. Preparation of OMC, BOMC, Pt-OMC and Pt-BOMC

SBA-15, the silica template, was synthesized using Pluronic P123 as the surfactant and tetraethyl orthosilicate as the silica precursor [48]. The OMC was prepared according to the method reported by Jun and coworkers, using SBA-15 and sucrose as template and carbon precursor, respectively [19]. The BOMC was prepared by adjusting the mass ratio of 4-hydroxyphenylboronic acid/sucrose to 0.15. In order to extensively dissolve the remaining boron oxide, the obtained BOMC was further boiled in deionized water at 100 °C for 6 h [34].

To prepare Pt-BOMC, 25 mg of BOMC was dispersed in 20 mL of double distilled water containing 13 mg of $H_2PtCl_6{\cdot}6H_2O$ and the mixture was sonicated for about 30 min. After that, 2 mL of HCOOH was added dropwise with ultrasonication and the solution was kept at room temperature. After 72 h, the product was collected and washed several times with double distilled water, and dried at 70 °C. The Pt-OMC was prepared in the same way by using OMC instead of BOMC.

2.4. Electrode preparation and modification

GCE (3 mm diameter) was polished with 1, 0.3 and 0.05 μm alumina powders, respectively, rinsed thoroughly with double-distilled water between each polishing step, then ultrasonically cleaned with double-distilled water, and dried with nitrogen stream. BOMC/GCE was prepared by casting 5 μL of BOMC suspension (1 mL of N,N′-dimethylformamide (DMF) and 0.5 mg of BOMC) on the pretreated GCE surface, and dried under an infrared lamp. The preparation of OMC/GCE was done in the same way as BOMC/GCE.

Glucose oxidase (GOx) was used for glucose detection. To obtain BOMC/GOx/Nafion/GC electrode, 5 μL of GOx solution (10 mg mL^{-1}) was loaded onto the BOMC/GC electrode and the modified electrode was dried in a refrigerator at 4 °C. After drying, 5 μL of 0.5 wt.% Nafion solution was dropped on the modified electrode surface and dried also at 4 °C. The OMC/GOx/Nafion/GC electrode was made correspondingly.

Pt-BOMC/GCE was prepared by depositing 5 μL of Pt-BOMC suspension (2 mg of Pt-BOMCs and 1 mL of 0.5 wt.% Nafion solution)

on the well-cleaned GCE surface and the modified electrode was dried at room temperature. The Pt-OMC/GCE was obtained using the same procedure by using Pt-OMC suspension.

3. Results and discussion

3.1. Characterization

3.1.1. Characterization of BOMC

The morphologies and structures of OMC and BOMC were characterized by SEM and TEM. The TEM image of OMC (Fig. 1a) shows the hexagonal honeycomb-like arrangement of mesopores of OMC. The SEM analysis (inset of Fig. 1a) indicates that OMC is made of rod-like particles. Fig. 1b shows the TEM image of BOMC and displays the mesoporous honeycomb structure of BOMC. On the SEM image of BOMC (inset of Fig. 1b), it is shown that BOMC is composed of rode-like particles. The BOMC is the replica of SBA-15 template. From these results, it is demonstrated that the ordered mesoporous structure was maintained well after the incorporation of B.

Fig. 1c shows the nitrogen adsorption–desorption isotherms and the corresponding pore size distribution curves of OMC and BOMC. From the nitrogen adsorption isotherms, the specific surface area, pore volume and pore size distribution, were calculated. The nitrogen adsorption–desorption isotherm of OMC shows a type IV curve with a Brunauer–Emmett–Teller (BET) surface area of 1255 $m^2 g^{-1}$ (black line in Fig. 1c), a total pore volume of 1.55 $cm^3 g^{-1}$, and the pore size of 5.0 nm (black line in the inset of Fig. 1c). The nitrogen adsorption data of BOMC present a type IV isotherm with BET surface area of 900 $m^2 g^{-1}$ (red line in Fig. 1c), total pore volume of 1.24 $cm^3 g^{-1}$, and the pore size of 6.4 nm (red line in the inset of Fig. 1c). These results reveal that the incorporation of B into the framework of OMC leads to a decrease in the specific surface area and pore volume of OMC.

The small-angle XRD patterns of OMC and BOMC are shown in Fig. 1d. The small-angle XRD of OMC (black line) displays three well-resolved diffraction peaks, which correspond to (100), (110), and (200) reflections of two-dimensional hexagonal arrangements. The small-angle XRD pattern of BOMC (red line) shows also three well-resolved peaks, corresponding to the (100), (110), and (200) reflections of the 2-dimensional hexagonal

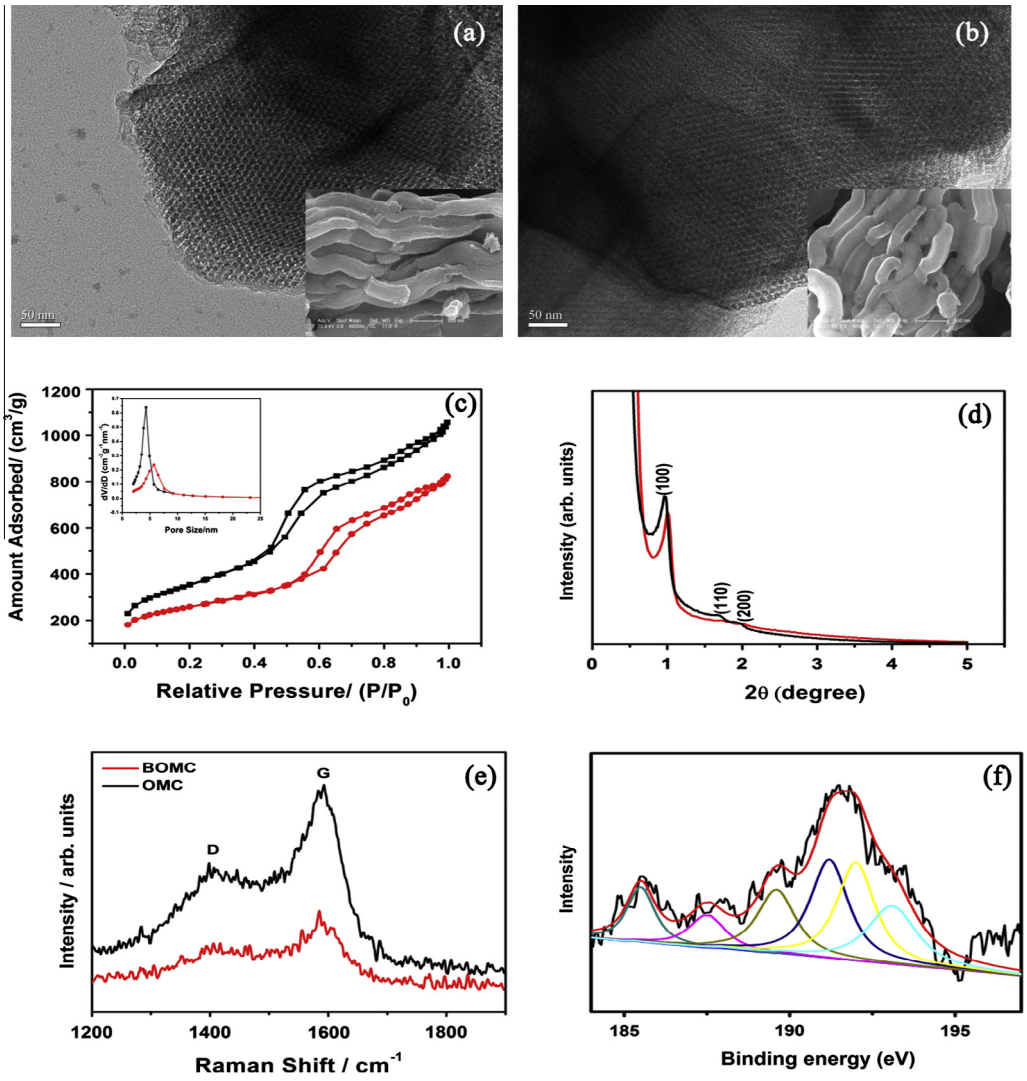

Fig. 1. (a) TEM image of OMC. Inset: SEM image of OMC. (b) TEM image of BOMC. Inset: SEM image of BOMC. (c) Nitrogen adsorption–desorption isotherms of OMC (black line) and BOMC (red line). Inset: Pore size distributions of OMC (black line) and BOMC (red line). (d) Small-angle XRD patterns of OMC (black line) and BOMC (red line). (e) Raman spectra of OMC (black line) and BOMC (red line). (f) High-resolution B 1s core-level XPS spectrum of BOMC. (For interpretation of the references to color in this figure legend, the reader is referred to the web version of this article.)

mesostructure. This confirms that the synthesized BOMC is the replica of the parent template which is SBA-15. Compared with OMC, the (1 0 0) peak of BOMC shows a shift toward large angle, indicating the decrease in cell parameter after the doping of B.

Raman spectroscopy was used to observe the structural changes brought by boron doping in OMC. Fig. 1e shows the Raman spectra of OMC (black line) and BOMC (red line), in which a strong peak at about 1590 cm^{-1} (G-band) and a weak peak at 1397 cm^{-1} (D-band) can be clearly seen. The observed D and G bands, in both OMC and BOMC spectra, correspond to defects and hexagonal graphene plane, respectively. This means that the relative intensity ratio of the D and G bands (I_D/I_G ratio) is proportional to the number of defect sites in graphite carbon [34,40,49]. The I_D/I_G ratio of BOMC (2.39) is larger than that of OMC (2.01), indicating the introduction of defects and imperfections into carbon lattice by boron doping.

The presence of B in BOMC was investigated by XPS. The detailed B1s XPS spectra of the BOMC sample, which are evident for the existence of boron heteroatoms in the forms of different bonds, are shown in Fig. 1f. From the B1s XPS spectra, it is clearly shown that there are six peaks at 185.5 (B cluster, blue–green line), 187.5 (B_4C, purple line), 189.6 (BC_3, olive line), 191.2 (BC_2O, dark-blue line), 192.1 (BCO_2, yellow line) and 193.1 eV (B_2O_3, cyan line) [34,45]. The presence of B_2O_3 may due to the decomposition of a small amount of un-reacted boric acid in the carbonization process. The binding energy indicates that boron is bonded to carbon in the sp^2 carbon network. The incorporation of boron can disrupt sp^2 hybridization of carbon framework. The presence of the B–C bonding in deconvoluted B1s signals provides evidence for the replacement of C atoms within the BOMC sheet by highly coordinated boron dopants. The result demonstrates that boron with content of 1.3 at.% can be doped into the framework of BOMC. These results from XPS analysis confirm that B atoms were doped into the framework of OMC.

3.1.2. Characterization of Pt-BOMC

The property of BOMC of acting as support for noble metal nanoparticle catalysts was also investigated. Pt, as one of the most used noble metal catalysts, was employed in this study. In practical usage, Pt nanoparticles are generally dispersed with a conducting support in order to avoid their agglomerations and keep their activities [15]. In this work, the Pt nanoparticles were incorporated in the pores of BOMC and that incorporation was proved by the characterization of the resulting Pt-BOMC.

The structural characterization of Pt-BOMC is shown in Fig. 2. Fig. 2a and b shows the TEM images of Pt-OMC (a) and Pt-BOMC (b), and the insets indicate the particle size distribution of the Pt nanoparticles on the OMC (inset of Fig. 2a) and on BOMC (inset of Fig. 2b). As shown in the histograms, the average diameter of 100 particles on Pt-OMC was found to be 4.36 nm and that of 100 particles on Pt-BOMC is 2.62 nm. It can be seen that Pt nanoparticles on OMC tend to aggregate and form large particle clusters. In contrast, the Pt nanoparticles on BOMC are uniformly distributed with good dispersion. More defective sites are responsible for high dispersion of Pt nanoparticles on BOMC. The XPS patterns of Pt 4f for Pt-BOMC (Fig. 2c) confirm the presence of Pt nanoparticles on BOMC. TGA was used to determine the content of the Pt nanoparticles in Pt-OMC and Pt-BOMC. Fig. 2d shows the TGA of Pt-OMC (red line) and Pt-BOMC (black line). The results show that the weight of Pt is around 10% in Pt-OMC and Pt-BOMC.

Pt-OMC/GCE and Pt-BOMC/GCE were characterized electrochemically in N_2-saturated 0.5 M H_2SO_4 solution at the scan rate of 50 mV s^{-1} (Fig. 3). The electrochemical surface area (ECSA) of the Pt nanoparticles supported on the OMC and BOMC was calculated by integrating the total charge corresponding to the adsorption peak of hydrogen, and normalizing with scan rate, Pt loading, and the charge value of 210 μC cm^{-2} for Pt surface. The obtained results show that the ECSA of Pt-BOMC (112.178 $m^2\,g^{-1}$) is

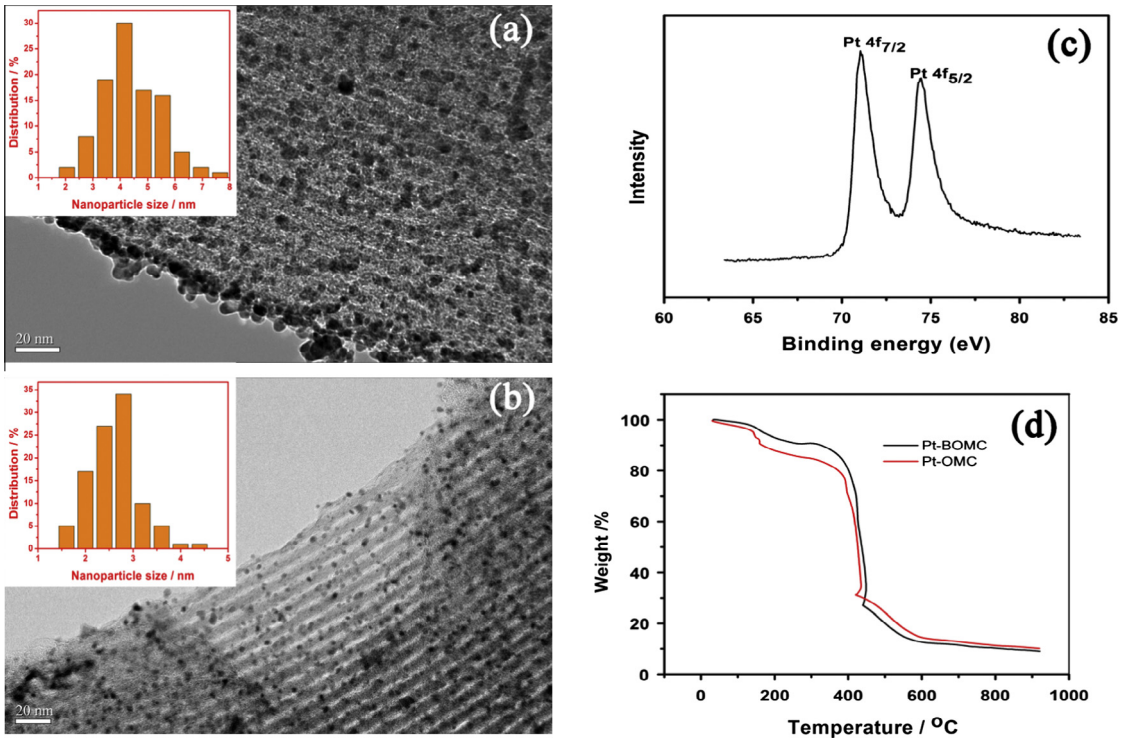

Fig. 2. (a) TEM images of Pt-OMC. Inset indicates the particle size distribution of the Pt nanoparticles on the OMC. (b) TEM images of Pt-BOMC. Inset indicates the particle size distribution of the Pt nanoparticles on the BOMC. (c) XPS patterns of Pt 4f for Pt-BOMC. (d) TGA of Pt-BOMC (black line) and Pt-OMC (red line). (For interpretation of the references to color in this figure legend, the reader is referred to the web version of this article.)

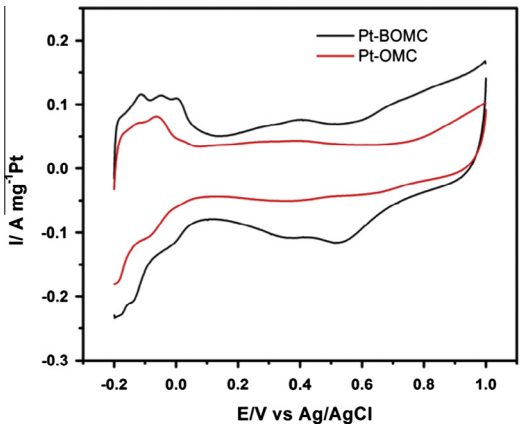

Fig. 3. CVs of Pt-BOMC/GCE (black line) and Pt-OMC/GCE (red line) under N_2 atmosphere 0.5 M H_2SO_4 at the scan rate of 50 mV s^{-1}. (For interpretation of the references to color in this figure legend, the reader is referred to the web version of this article.)

approximately 2.1 times larger than that of Pt-OMC (53.54 m^2 g^{-1}). The presence of the defect sites on the BOMC provides strong interaction with Pt and serves as anchor sites for the heterogeneous nucleation of Pt. The doping of boron leads to a uniform deposition of Pt nanoparticles on BOMC and thus high electrochemical surface area.

3.2. Electrochemical response of BOMC/GE to different biomolecules

The electrocatalytic activity of BOMC was investigated by comparing the electrochemical response of BOMC/GCE with that of OMC/GCE to different biomolecules. AA, or vitamin C, is important as an antioxidant and participates in numerous cellular functions [50]. It is also a powerful antioxidant in food, preventing color changes and alterations of aroma and flavor and extending the storage time of the products [51]. DA is one of the most important neurotransmitters and it plays a significant role in the functioning of central nervous, renal and hormonal systems [13]. The research has shown that the abnormal levels of UA in the body are symptom of several diseases such as gout, Lesch–Nyan syndrome, cardiovascular and kidney damages [24,52]. H_2O_2 has wide applications in industrial processes, and it is a very important intermediate in environmental and biological reactions. It is one of the most important analytes in the field of electroanalysis as it is cytotoxic, an indicator of oxidative stress and the product of several enzyme-catalyzed reactions [53–55]. NADH is involved as a cofactor in several hundred enzymatic reactions of NAD^+/NADH-dependent dehydrogenases [42,56]. Its determination is very important because NADH and its oxidized form (NAD^+) are the coenzymes for a large number of dehydrogenase enzymes and components of biomarker systems [57–59].

Table 1
Table of summary of cyclic voltammetry data of AA, DA and UA, obtained at GCE, OMC/GCE and BOMC/GCE.

	GCE		OMC/GCE		BOMC/GCE	
	E_p (V)	I_p (μA)	E_p (V)	I_p (μA)	E_p (V)	I_p (μA)
AA	0.217	23.260	0.020	38.175	−0.006	56.270
UA	0.373	4.766	0.319	16.860	0.318	30.810
DA	0.237	48.934	0.222	81.133	0.221	123.298

Fig. 4a–c shows the CVs for AA (a), DA (b) and UA (c) at GCE, OMC/GCE and BOMC/GCE. The obtained results are summarized in Table 1. It is seen that BOMC/GCE (a3) exhibits a negatively shifted potential and a rapidly increasing peak current compared with OMC/GCE (a2) activity toward AA. Different from DA and UA oxidations, only the sharply increased peak currents are observed at BOMC/GCE (b3 and c3) compared with OMC/GCE (b2 and c2). These results show that BOMC/GCE exhibits different electrochemical behavior to different molecules. The change in OMC's properties by introduction of B into its framework may be the cause of this electrocatalytic behavior of BOMC. Such enhanced electrocatalytic performance of BOMC can be the basis of the fabrication of highly effective electrochemical sensors.

The generation of edge plane like-sites or defects is observed after doping in BOMC. It has been reported that carbon materials with high edge plane sites or defects possess a high density of electronic states, which is the key factor in determining the heterogeneous electron transfer rate of electrode [43,46]. The pristine OMC has low defective sites and there are no dangling bonds because the carbon atoms have satisfied valances. When boron is introduced, the surface is disturbed and surface defects are introduced. The high density of electronic states at BOMC is increased through defective sites and then electroactive species exhibit increasing electron transfer rates.

In this study, H_2O_2 and NADH were detected by CV and amperometry at different electrodes. Fig. 5a and b shows CVs of 5 mM H_2O_2 and 5 mM NADH at GCE (a1 and b1), OMC/GCE (a2 and b2) and BOMC/GCE (a3 and b3) in 0.1 M PBS (pH 7.4) at the scan rate of 50 mV s^{-1}. The results show that the onset potentials of H_2O_2 oxidation on GCE, OMC/GCE and BOMC/GCE are 0.64 V, 0.45 V, and 0.38 V, respectively. The peak potentials of NADH oxidation are shifted from 0.60 V on GCE and 0.39 V on OMC/GCE to 0.21 V on BOMC/GCE. This indicates the superior electrochemical activity of BOMC/GCE toward H_2O_2 and NADH compared with that of OMC/GCE and GCE. The comparison of the amperometric responses of OMC/GCE and BOMC/GCE with successive additions of 0.1 mM H_2O_2 at +0.38 V and 0.1 mM NADH at +0.21 V is presented in Fig. 5c and d. As shown, BOMC/GCE exhibits faster responses after each addition of H_2O_2 compared with OMC/GCE, and it is the same for NADH. The corresponding calibration curves are shown in the insets of Fig. 5c and d. The sensitivities to H_2O_2 on OMC/GCE and

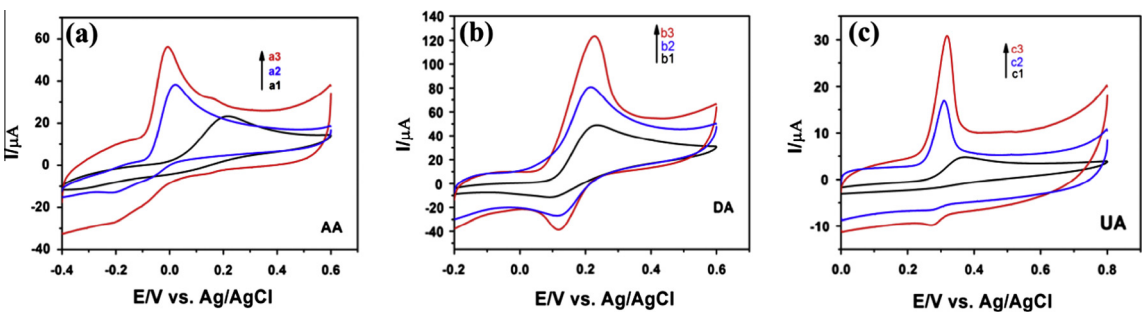

Fig. 4. (a) CVs for 2 mM AA at GCE (a1), OMC/GCE (a2) and BOMC/GCE (a3). (b) CVs for 2 mM DA at GCE (b1), OMC/GCE (b2) and OMC/GCE (b3). (c) CVs for 1 mM UA at GCE (c1), OMC/GCE (c2) and BOMC/GCE (c3). Supporting electrolyte: 0.1 M PBS (pH 7.4). Scan rate: 50 mV s^{-1}.

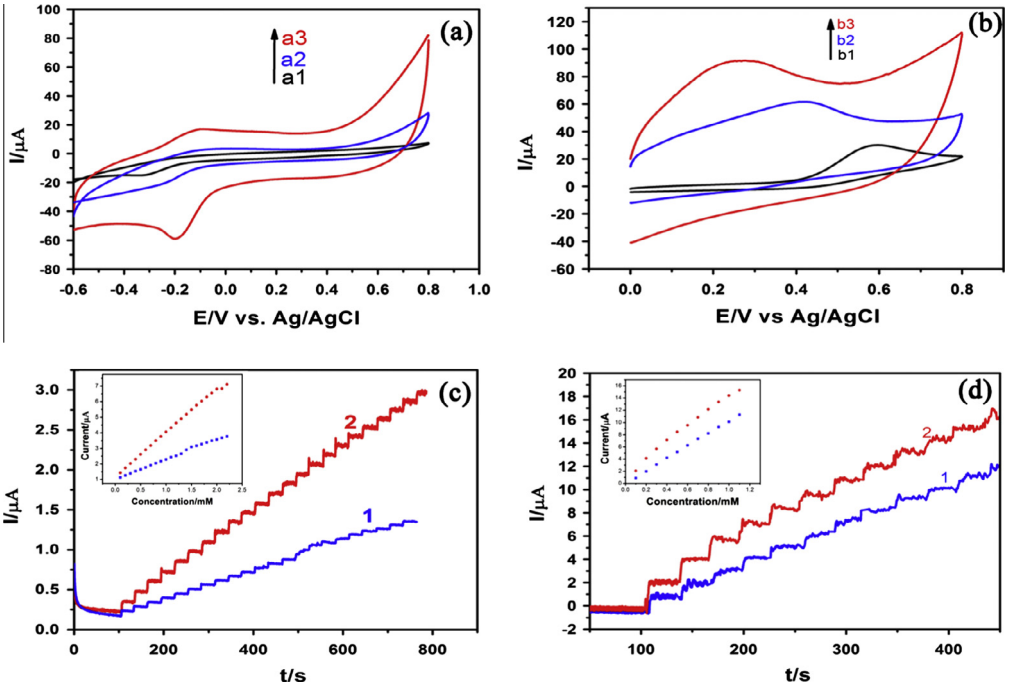

Fig. 5. (a) CVs of 5 mM H_2O_2 at GCE (a1), OMC/GCE (a2) and BOMC/GCE (a3). (b) CVs of 5 mM NADH at GCE (b1), OMC/GCE (b2) and BOMC/GCE (b3). Scan rate: 50 mV s^{-1}. (c) Current–time curves of OMC/GCE (1) and BOMC/GCE (2) at +0.38 V with successive additions of 0.1 mM H_2O_2. Inset: Calibration curves for H_2O_2 on OMC/GCE (blue) and BOMC/GCE (red). (d) Current–time curves of OMC/GCE (1) and BOMC/GCE (2) at +0.21 V with successive additions of 0.1 mM NADH. Inset: Calibration curves for NADH on OMC/GCE (blue) and BOMC/GCE (red). Supporting electrolyte: 0.1 PBS (pH 7.4). (For interpretation of the references to color in this figure legend, the reader is referred to the web version of this article.)

on BOMC/GCE are 1.301 and 2.769 μA mM^{-1}, respectively. The calculated detection limits of H_2O_2 on OMC/GCE and BOMC/GCE are 10.4 μM and 9.59 μM ($S/N = 3$), respectively. For NADH, the sensitivity on OMC/GCE is 10.290 μA mM^{-1} and on BOMC/GCE is 12.965 μA mM^{-1}. The corresponding detection limit of NADH on OMC/GCE is 116.3 μM and that on BOMC/GCE is 74.4 μM. From these results, it is seen that the performance of BOMC in the electrochemical detection of H_2O_2 and NADH is higher than that of OMC. It is possible that this is due to the electronic structure and pore size of BOMC brought by the incorporation of B into the framework of OMC, which might provide many active sites for electron transfer. The edge-plane-like defective sites may be also the source of that electrocatalytic behavior of BOMC [46]. The obtained results suggest that, from BOMC, the advanced H_2O_2 and NADH electrochemical sensors can be constructed.

The ability of BOMC of loading active biomolecules was investigated by using GOx. Fig. 6 shows the electrocatalytic behavior of BOMC/GOx/Nafion/GCE toward the electrochemical detection of glucose in 0.1 M PBS (pH 7.4). The electrocatalytic oxidation of glucose is important because of its medical application in blood glucose sensing and bio-fuel cells [46]. The detection of glucose can be based on H_2O_2 formed during enzyme-catalyzed reaction [60]:

$$\text{Glucose} + O_2 \xrightarrow{Gox} \text{Gluconic acid} + H_2O_2$$

Based on the higher performance of BOMC in H_2O_2 electrochemical detection compared with that of OMC, the direct electrochemical detection of glucose using BOMC was investigated.

As shown in Fig. 6a displaying the CVs, the BOMC/GOx/Nafion/GCE (red line), in oxygen-saturated PBS containing 20 mM glucose (pH 7.4) at the scan rate of 50 mV s^{-1}, exhibited a remarkable increase in the catalytic oxidation current compared with OMC/GOx/Nafion/GCE (blue line) and GOx/Nafion/GCE (black line). These results are consistent with that of CVs for the electrocatalytic oxidation of H_2O_2 (Fig. 5a). This reveals that the improved electrochemical reactivity was accomplished on BOMC/GOx/Nafion/GCE. Fig. 6b shows the amperometric responses obtained at +0.38 V for OMC/GOx/Nafion/GCE (1) and BOMC/GOx/Nafion/GCE (2) with successive additions of 0.5 mM glucose in stirred PBS. It can be seen from Fig. 6b that the amperometric response for BOMC/GOx/Nafion/GCE is higher than that for OMC/GOx/Nafion/GCE. The corresponding calibration plots recorded on OMC/GOx/Nafion/GCE and BOMC/GOx/Nafion/GCE are shown in the inset of Fig. 4b. The sensitivities to glucose on OMC/GOx/Nafion/GCE and BOMC/GOx/Nafion/GCE are 0.487 and 1.074 μA mM^{-1}, respectively. The detection limit of glucose to around 39 μM for BOMC/GOx/Nafion/GCE is much lower than 278 μM for OMC/GOx/Nafion/GCE. These results show the significantly enhanced performance on BOMC/GOx/Nafion/GCE for glucose detection compared with OMC/GOx/Nafion/GCE. This enhanced performance is due to the high electrocatalyitc activity for H_2O_2 at BOMC. It can be also attributed to the physical and chemical structure of BOMC, resulting from the B doping, which would improve greatly the direct electron transfer between the adsorbed GOx and the electrode. From these observations, we can conclude that BOMC may be a candidate for fabricating the promising glucose sensors.

3.3. Electrocatalytic oxidation of methanol at Pt-BOMC/GCE

The electrocatalytic behavior of Pt-BOMC was studied by investigating its electrocatalytic activity in the direct methanol oxidation reaction. Pt-BOMC was compared with Pt-OMC and commercial Pt-C catalyst. Fig. 7a shows the CVs of Pt-BOMC/GCE (black line), Pt-OMC/GCE (red line) and Pt-C/GCE (blue line), in a 0.5 M H_2SO_4 solution with 1 M methanol at 50 mV s^{-1}. It can be seen that the activity of Pt-OMC is higher than that of commercial Pt-C catalyst. Compared with Pt-OMC, a significant negative peak potential and high peak current density can be observed on Pt-BOMC. The oxidation peak potentials at Pt-C/GCE, Pt-OMC/GCE

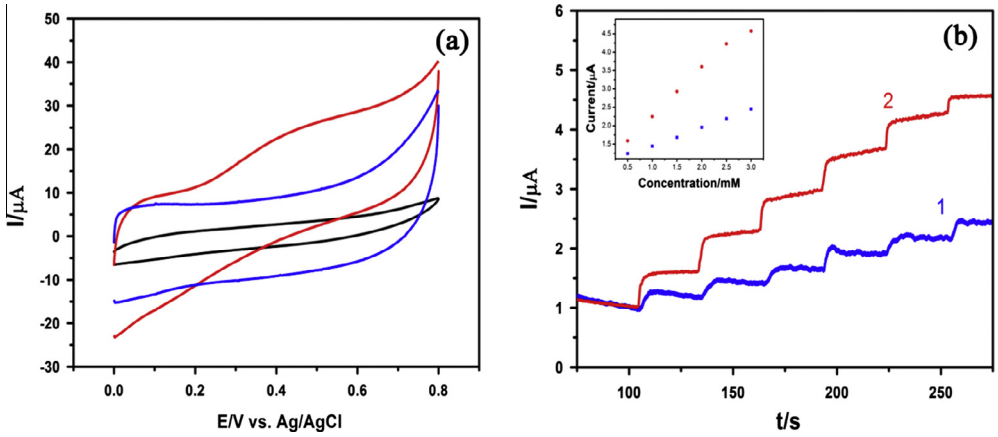

Fig. 6. (a) CVs of 20 mM Glucose at GOx/Nafion/GCE (black line), OMC/GOx/Nafion/GCE (blue line) and BOMC/GOx/Nafion/GCE (red line). Scan rate: 50 mV s^{-1}. (b) Current–time curves of OMC/GOx/Nafion/GCE (1) and BOMC/GOx/Nafion/GCE (2) at +0.38 V with successive additions of 0.5 mM of glucose in air-saturated 0.1 M PBS pH 7.4. Inset: Calibration curves for glucose on OMC/GOx/Nafion/GCE (blue) and BOMC/GOx/Nafion/GCE (red). (For interpretation of the references to color in this figure legend, the reader is referred to the web version of this article.)

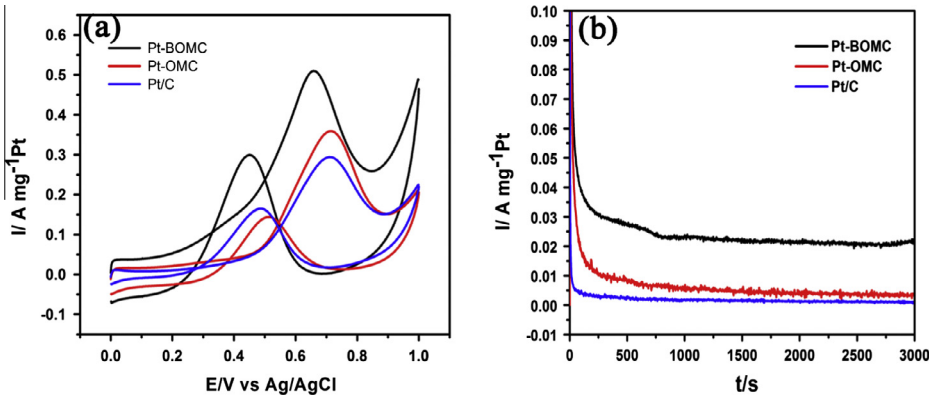

Fig. 7. (a) CVs of Pt-BOMC/GCE (black line), Pt-OMC/GCE (red line) and Pt-C/GCE (blue line) in a 0.5 M H_2SO_4 solution with 1 M methanol at the scan rate of 50 mV s^{-1}. (b) Chronoamperometric responses for the oxidation of methanol at 0.658 V on Pt-BOMC/GCE (black line), Pt-OMC/GCE (red line) and Pt-C/GCE (blue line). (For interpretation of the references to color in this figure legend, the reader is referred to the web version of this article.)

and Pt-BOMC/GCE are 0.717 V, 0.710 V, and 0.658 V, respectively. The peak values of the oxidation current density are 0.294 A mg^{-1} at Pt-C/GCE, 0.360 A mg^{-1} at Pt-OMC/GCE, and 0.511 A mg^{-1} at Pt-BOMC/GCE.

The chronoamperometric responses of Pt-C/GCE, Pt-OMC/GCE and Pt-BOMC/GCE for methanol oxidation at 0.658 V, are shown in Fig. 7b. The current density for Pt-BOMC (black line) at 3000s is 6.64 times greater than that of the Pt-OMCs (red line) and 19.93 times greater than that of Pt-C (blue line) for the oxidation of methanol. The highly remarkable electrocatalytic performance of Pt-BOMC can be due to the better dispersion and utilization of Pt particles, electrochemical surface area, as well as a stronger Pt-support interaction in the Pt-BOMC catalyst. The synergetic effect between Pt and BOMC may be the source of the highly enhanced performance of Pt-BOMC in the electrocatalysis of methanol oxidation.

4. Conclusion

The electrochemical properties of BOMC as an electrode material and Pt catalysts support were investigated. The TEM, SEM, BET specific surface area, XRD, Raman spectroscopy, and XPS studies showed the structure of BOMC. The electrochemical behaviors of different electroactive compounds were studied at BOMC/GCE, which exhibited higher electrochemical activity than OMC/GCE and GCE. The ability of BOMC of loading active biomolecules was investigated by using glucose oxidase. BOMC showed higher sensitivities and lower detection limits toward H_2O_2, NADH and glucose electrochemical detection compared with OMC. It was found that BOMC supports Pt nanoparticles more efficiently than OMC. The average diameter of Pt particles on Pt-BOMC was found to be 2.62 nm. The structure and electrocatalytic activity of the obtained Pt-BOMC were studied. The Pt-BOMC's activity in the electrocatalysis of methanol oxidation reaction was found to be remarkably higher than that of Pt-OMC and commercial Pt-C catalyst. This enhanced performance of BOMC may be attributed to its structural characteristics and the synergetic effect between boron and OMC. All those facts suggest that BOMC is an electrode material for the construction of various promising electrochemical devices.

Acknowledgments

The authors gratefully acknowledge the financial support of the National Natural Science Foundation of China (21075014) and the Fundamental Research Funds for the Central Universities (No. 10SSXT141).

References

[1] R. Ryoo, S.H. Joo, S. Jun, J. Phys. Chem. B 103 (1999) 7743.
[2] J.C. Ndamanisha, L. Guo, Anal. Chim. Acta 747 (2012) 19.
[3] A. Walcarius, TrAC, Trends Anal. Chem. 38 (2012) 79.
[4] A. Walcarius, Chem. Soc. Rev. 42 (2013) 4098.

[5] L. Zhu, C. Tian, D. Yang, X. Jiang, R. Yang, Electroanalysis 20 (2008) 2518.
[6] J. Bai, B. Lu, X. Bo, L. Guo, Electrochem. Commun. 12 (2010) 1563.
[7] J. Zeng, C. Francia, C. Gerbaldi, V. Baglio, S. Specchia, A.S. Aricò, P. Spinelli, Electrochim. Acta 94 (2013) 80.
[8] L. Zhou, X. Liu, J. Li, N. Wang, Z. Wang, Y. Zhou, Chem. Phys. Lett. 413 (2005) 6.
[9] X. Zhuang, Y. Wan, C. Feng, Y. Shen, D. Zhao, Chem. Mater. 21 (2009) 706.
[10] X. Yuan, S.P. Zhuo, W. Xing, H.Y. Cui, X.D. Dai, X.M. Liu, Z.F. Yan, J. Colloid Interface Sci. 310 (2007) 83.
[11] X. Wang, J.S. Lee, Q. Zhu, J. Liu, Y. Wang, S. Dai, Chem. Mater. 22 (2010) 2178.
[12] L.-B. Kong, H. Li, J. Zhang, Y.-C. Luo, L. Kang, Appl. Surf. Sci. 256 (2010) 6688.
[13] N. Jia, Z. Wang, G. Yang, H. Shen, L. Zhu, Electrochem. Commun. 9 (2007) 233.
[14] L. Luo, F. Li, L. Zhu, Z. Zhang, Y. Ding, D. Deng, Electrochim. Acta 77 (2012) 179.
[15] X. Jiang, Y. Wu, X. Mao, X. Cui, L. Zhu, Sens. Actuators, B 153 (2011) 158.
[16] W. Xing, S.Z. Qiao, R.G. Ding, F. Li, G.Q. Lu, Carbon 44 (2006) 216.
[17] C. Vix-Guterl, E. Frackowiak, K. Jurewicz, M. Friebe, J. Parmentier, F. Béguin, Carbon 43 (2005) 1293.
[18] H. Chang, S.H. Joo, C. Pak, J. Mater. Chem. 17 (2007) 3078.
[19] S. Jun, S. Joo, R. Ryoo, J. Am. Chem. Soc. 122 (2000) 10712.
[20] J.C. Ndamanisha, J. Bai, B. Qi, L. Guo, Anal. Biochem. 386 (2009) 79.
[21] D. Banham, F. Feng, T. Fürstenhaupt, K. Pei, S. Ye, V. Birss, J. Power Sources 196 (2011) 5438.
[22] L. Wang, X. Bo, J. Bai, L. Zhu, L. Guo, Electroanalysis 22 (2010) 2536.
[23] L. Liu, J.C. Ndamanisha, J. Bai, L.-P. Guo, Electrochim. Acta 55 (2010) 3035.
[24] J.C. Ndamanisha, L. Guo, Biosens. Bioelectron. 23 (2008) 1680.
[25] L. Liu, L.P. Guo, X.J. Bo, J. Bai, X.J. Cui, Anal. Chim. Acta 673 (2010) 88.
[26] L. Zhu, R. Yang, X. Jiang, D. Yang, Electrochem. Commun. 11 (2009) 530.
[27] D. Zheng, J. Ye, L. Zhou, Y. Zhang, C. Yu, Electroanalysis 21 (2009) 184.
[28] Y. Hou, J.C. Ndamanisha, L.-P. Guo, X.-J. Peng, J. Bai, Electrochim. Acta 54 (2009) 6166.
[29] X. Bo, J. Bai, L. Wang, L. Guo, Talanta 81 (2010) 339.
[30] J. Dong, Y. Hu, S. Zhu, J. Xu, Y. Xu, Anal. Bioanal. Chem. 396 (2010) 1755.
[31] Z. Zhu, X. Li, Y. Zeng, W. Sun, Biosens. Bioelectron. 25 (2010) 2313.
[32] D.S. Yang, D. Bhattacharjya, S. Inamdar, J. Park, J.S. Yu, J. Am. Chem. Soc. 134 (2012) 16127.
[33] X. Zhao, A. Wang, J. Yan, G. Sun, L. Sun, T. Zhang, Chem. Mater. 22 (2010) 5463.
[34] X. Bo, L. Guo, PCCP 15 (2013) 2459.
[35] X. Zhai, Y. Song, J. Liu, P. Li, M. Zhong, C. Ma, H. Wang, Q. Guo, L. Zhi, J. Electrochem. Soc. 159 (2012) E177.
[36] A. Lu, A. Kiefer, W. Schmidt, F. Schüth, Chem. Mater. 16 (2004) 100.
[37] S. Ding, S. Zheng, M. Xie, L. Peng, X. Guo, W. Ding, Microporous Mesoporous Mater. 142 (2011) 609.
[38] D.H. Zhong, H. Sano, Y. Uchiyama, K. Kobayashi, Carbon 38 (2000) 1199.
[39] X. Zhao, Q. Zhang, B. Zhang, C.-M. Chen, J. Xu, A. Wang, D.S. Su, T. Zhang, RSC Adv. 3 (2013) 3578.
[40] D.-W. Wang, F. Li, Z.-G. Chen, G.Q. Lu, H.-M. Cheng, Chem. Mater. 20 (2008) 7195.
[41] K. Peckova, J. Barek, Curr. Org. Chem. 15 (2011) 3014.
[42] T.N. Rao, I. Yagi, T. Miwa, D.a. Tryk, A. Fujishima, Anal. Chem. 71 (1999) 2506.
[43] Z.-H. Sheng, H.-L. Gao, W.-J. Bao, F.-B. Wang, X.-H. Xia, J. Mater. Chem. 22 (2012) 390.
[44] S. Wang, L. Zhang, Z. Xia, A. Roy, D.W. Chang, J.B. Baek, L. Dai, Angew. Chem., Int. Ed. 51 (2012) 4209.
[45] L. Yang, S. Jiang, Y. Zhao, L. Zhu, S. Chen, X. Wang, Q. Wu, J. Ma, Y. Ma, Z. Hu, Angew. Chem., Int. Ed. 50 (2011) 7132.
[46] X. Chen, J. Chen, C. Deng, C. Xiao, Y. Yang, Z. Nie, S. Yao, Talanta 76 (2008) 763.
[47] S. Wang, T. Cochell, A. Manthiram, PCCP 14 (2012) 13910.
[48] D. Zhao, J. Feng, Q. Huo, N. Melosh, Science 279 (1998) 548.
[49] M. Zhou, L. Shang, B. Li, L. Huang, S. Dong, Electrochem. Commun. 10 (2008) 859.
[50] J. May, Vitamin C Transport and its Role in the Central Nervous System, Springer, Netherlands, Dordrecht, 2012.
[51] I.G. Casella, Electroanalysis 8 (1995) 128.
[52] R.M.A. Tehrani, S. Ab Ghani, Sens. Actuators, B 145 (2010) 20.
[53] A. Chen, S. Chatterjee, Chem. Soc. Rev. 42 (2013) 5425.
[54] A. Salimi, M. Mahdioun, A. Noorbakhsh, A. Abdolmaleki, R. Ghavami, Electrochim. Acta 56 (2011) 3387.
[55] Y. Zhang, X. Bo, A. Nsabimana, C. Luhana, G. Wang, H. Wang, M. Li, L. Guo, Biosens. Bioelectron. 53 (2014) 250.
[56] C. Shan, H. Yang, D. Han, Q. Zhang, A. Ivaska, L. Niu, Biosens. Bioelectron. 25 (2010) 1504.
[57] A. Arvinte, F. Valentini, A. Radoi, F. Arduini, E. Tamburri, L. Rotariu, G. Palleschi, C. Bala, Electroanalysis 19 (2007) 1455.
[58] C.E. Banks, R.G. Compton, Analyst 130 (2005) 1232.
[59] G.P. Keeley, A. O'Neill, M. Holzinger, S. Cosnier, J.N. Coleman, G.S. Duesberg, PCCP 13 (2011) 7747.
[60] J. Wang, Chem. Rev. 108 (2008) 814.